Inner-Shelf Response to Cross-Shelf Wind Stress: The Importance of the Cross-Shelf Density Gradient in an Idealized Numerical Model and Field Observations

RACHEL HORWITZ AND STEVEN J. LENTZ

Woods Hole Oceanographic Institution, Woods Hole, Massachusetts

(Manuscript received 31 March 2013, in final form 12 September 2013)

ABSTRACT

This study investigates the effects of horizontal and vertical density gradients on the inner-shelf response to cross-shelf wind stress by using an idealized numerical model and observations from a moored array deployed south of Martha's Vineyard, Massachusetts. In two-dimensional (no along-shelf variation) numerical model runs of an initially stratified shelf, a cross-shelf wind stress drives vertical mixing that results in a nearly well-mixed inner shelf with a cross-shelf density gradient because of the sloping bottom. The cross-shelf density gradient causes an asymmetric response to on- and offshore wind stresses. For density increasing offshore, an offshore wind stress drives a near-surface offshore flow and near-bottom onshore flow that slightly enhances the vertical stratification and the cross-shelf circulation. An onshore wind stress drives the reverse cross-shelf circulation reducing the vertical stratification and the cross-shelf circulation. A horizontal Richardson number is shown to be the nondimensional parameter that controls the dependence of the wind-driven nondimensional cross-shelf transport on the cross-shelf density gradient. Field observations show the same empirical relationship between the horizontal Richardson number and transport fraction as the model predicts. These results show that it is the cross-shelf rather than vertical density gradient that is critical to predicting the inner-shelf cross-shelf transport driven by a cross-shelf wind stress.

1. Introduction

Transport across continental shelves allows the exchange of heat, nutrients, larvae, sediment, and pollutants between coastal ecosystems and the open ocean. The inner shelf is a critical link in the cross-shelf transport pathway, connecting the surfzone and the continental shelf, but the mechanisms that drive cross-shelf circulation on the inner shelf are not well understood. On mid- and outer shelves, along-shelf winds typically drive cross-shelf transport following classic Ekman (1905) theory. Where the water is shallower, momentum from the wind mixes to the bottom faster than the Coriolis acceleration can turn it, so the along-shelf wind stress is ineffective at driving cross-shelf transport (Ekman 1905; Austin and Lentz 2002; Lentz and Fewings 2012). This region where the entire water column is filled by turbulent surface and bottom boundary layers is often referred to as the inner shelf.

Regional-scale studies have suggested cross-shelf winds as potentially able to complete the transport pathway between the surfzone and midshelf (Li and Weisberg 1999a,b; Cudaback et al. 2005; Estrade et al. 2008). Recent observational (Fewings et al. 2008) and modeling (Tilburg 2003) studies focused specifically on the cross-shelf wind stress have shown it to be a significant mechanism for cross-shelf transport on the inner shelf. Using a 2D idealized numerical model (no along-shelf variation), Tilburg (2003) demonstrated that when wind stress blows toward the coast, water near the surface moves onshore. As water piles up at the coast, a pressure gradient grows to balance the wind stress, and that pressure gradient drives an offshore return flow in the lower portion of the water column (Fig. 1), a result consistent with the Ekman (1905) solution for cross-shelf wind stress. For offshore winds, the circulation is reversed, with offshore flow near the surface and an onshore return flow below. Fewings et al. (2008) described observations of this circulation using wintertime measurements from the Martha's Vineyard Coastal Observatory (MVCO). In winter, when the water column is presumably unstratified at 12-m water depth, Fewings et al. (2008) found cross-shelf wind stress to be

Corresponding author address: Rachel Horwitz, Department of Marine Sciences, University of Connecticut, Avery Point, 1080 Shennecossett Road, Groton, CT 06340.
E-mail: rhorwitz@uconn.edu

DOI: 10.1175/JPO-D-13-075.1

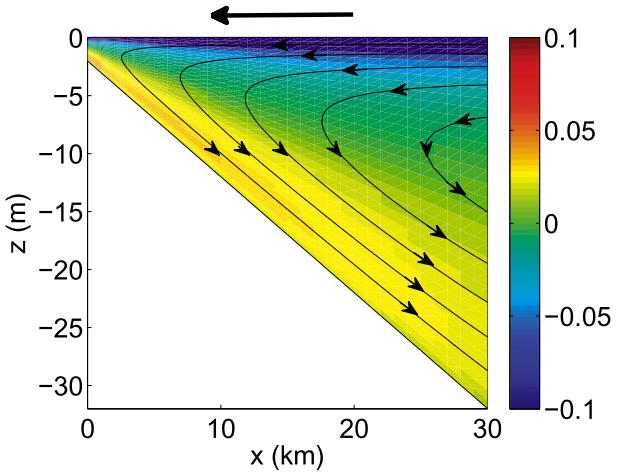

FIG. 1. Cross-shelf velocity (color; $\mathrm{m\,s^{-1}}$) and streamlines for streamfunction ψ [0.04 interval for $\psi/(\tau^{sx}/\rho_o f)$] for unstratified conditions and a 0.1 Pa wind stress.

far more effective at driving cross-shelf transport than along-shelf wind stress. Using a simple 2D unstratified numerical model, Fewings et al. (2008) also predicted that the region where cross-shelf wind is dominant should extend to around 30-m water depth for a 0.1 Pa wind stress in unstratified conditions.

A scale for the transport can be estimated as the product of the velocity and vertical length scales. The surface wind stress τ^s provides the relevant velocity scale, the shear velocity $u_*^2 \equiv \tau^s/\rho_o$, where ρ_o is reference seawater density. In the deep-water limit and away from coastal boundaries, the turbulent boundary layer thickness provides the relevant vertical length scale. In unstratified conditions, the vertical length scale is $\delta_{\mathrm{Ek}} = \kappa u_*/f$ (Madsen 1977), which includes the empirically derived von Kármán constant $\kappa = 0.41$ and the Coriolis parameter f. Boundary layer transport then scales like the velocity scale times the vertical length scale $U \sim u_* \delta_{\mathrm{Ek}} \sim u_*^2/f$. Ekman (1905) showed that, for transport to the right of the wind stress, the proportionality constant is exactly one and $U = u_*^2/f$. For downwind transport, which is found by integrating to the first zero crossing of the cross-shelf velocity profile, the proportionality constant depends on the vertical mixing (Tilburg 2003; Lentz and Fewings 2012).

In the shallow-water limit, the water depth h is much less than the turbulent boundary layer thickness so the water depth is the relevant vertical length scale. The transport scales as the velocity scale times the vertical length scale $U \sim u_* h$. Lentz and Fewings (2012) demonstrated that transport at three Mid-Atlantic Bight inner-shelf sites follows this scaling. They found the fraction of the deep-water Ekman transport was proportional to water depth:

$$\frac{U}{\tau^{sx}/\rho_o f} \sim \frac{h}{\delta_{\mathrm{Ek}}}. \tag{1}$$

By writing τ^{sx}/ρ_o and δ_{Ek} as function of u_* and f, we find again that

$$U \sim \frac{h}{\delta_{\mathrm{Ek}}} \frac{\tau^{sx}}{\rho_o f} \sim \frac{hf}{u_*} \frac{u_*^2}{f} = u_* h. \tag{2}$$

Lentz and Fewings (2012) also found that velocity profiles from the North Carolina inner shelf collapsed together when velocity u was normalized by u_* and vertical coordinate z by water depth h, and were consistent with predictions from an unstratified 2D model (Lentz 1995).

Between the deep- and shallow-water limits, Ekman (1905) described the solution as a superposition of the two limits. The vertical length scale will be some function of both h and δ_{Ek} and the transition from deep to shallow defined by the ratio of the two vertical scales h/δ_{Ek}. For typical inner-shelf values of $f = 10^{-4}\,\mathrm{s^{-1}}$, $h = 10\,\mathrm{m}$, and $u_* = 0.01\,\mathrm{m\,s^{-1}}$, this ratio, $h/\delta_{\mathrm{Ek}} = 0.25$. We proceed with our analysis by taking the inner-shelf region to behave as the shallow-water limit predicts, while recognizing that rotation plays a small but perhaps nonnegligible role in the dynamics.

Though continental shelves are typically stratified much of the year and often have buoyant river plumes flowing alongshore, the inner-shelf response to cross-shelf winds over vertical and horizontal density gradients is still unclear. In water deeper than the surface boundary layer thickness, Tilburg (2003) found that stratification decreased cross-shelf transport by cross-shelf winds in the upper portion of the surface boundary layer by limiting the depth of the surface boundary layer, causing the Ekman spiral to turn back on itself sooner. However, Tilburg's analysis did not address the influence of the initial stratification, or the resulting density field after wind mixing, on the cross-shelf transport on the inner shelf (water shallower than the surface boundary layer thickness). South of Martha's Vineyard, Massachusetts, Fewings et al. (2008) noticed an increased vertical shear in the cross-shelf circulation and, for offshore wind stress, an increased transport in summertime. Summer is when their field site is typically stratified, but Fewings et al. (2008) did not have density data to accompany the velocity measurements. One other recent observational study (Dzwonkowski et al. 2011) used seasonal averages of velocity and density from the Alabama shelf to conclude that cross-shelf flow was most clearly correlated with cross-shelf wind stress in the fall and winter, when the water was least stratified.

Here, we use a numerical model of an idealized, 2D, cross-shelf transect to describe the effects of initial stratification, wind stress magnitude, surface heat flux, and cross-shelf density gradient, on the inner-shelf response to a cross-shelf wind stress. These factors are all common in field settings but difficult to isolate in observations. We demonstrate that the cross-shelf density gradient is an important control on the cross-shelf transport driven by cross-shelf winds and that the cross-shelf density gradient causes an asymmetric response to on- and offshore wind stresses. Observations from the inner shelf south of Martha's Vineyard are used to verify the model predictions.

Section 2 describes the Regional Ocean Modeling System (ROMS) model setup; section 3 describes the field program and data processing; section 4 presents numerical experiments varying wind stress magnitude and initial stratification using the same set of forcing conditions as Tilburg (2003), while focusing on the circulation on the inner rather than midshelf; in section 5, a relationship between the cross-shelf density gradient and model inputs is derived; section 6 isolates the effect of the cross-shelf density gradient on transport; section 7 compares field observations to model results; and section 8 concludes with a discussion and summary of the results.

2. Numerical model

We use ROMS (Shchepetkin and McWilliams 2005) to simulate inner-shelf dynamics. This section describes the numerical model, physical parameters selected for the ''base case,'' and the conditions varied over subsequent suites of model runs.

a. ROMS model

ROMS is a free-surface, terrain-following, primitive equations ocean model with a curvilinear orthogonal horizontal grid and a stretched terrain-following vertical grid based on Shchepetkin and McWilliams (2005). Time steps are 10 s for the barotropic part of the equations and 50 or 100 s for the baroclinic terms. All experiments were run for 5 model days with variables saved hourly.

1) GRID

The model domain is a periodic channel with sloping boundaries to represent two along-shelf uniform coastal regions that span from just outside the surfzone to the mid continental shelf. The cross-shelf section has a shallow coastal wall ($h_o = 2$ m) at each boundary. Depth increases away from each wall at a constant slope (10^{-3} for the base case) until the bathymetry reaches its maximum depth (65 m for the base case) at 63 km from the wall. The two sloping boundaries are separated by a 45-km-wide uniform depth region in the center of the domain for a total domain width of 171 km. The stretched vertical grid has 32 levels with enhanced resolution near the surface and bottom. Vertical grid spacing ranges from 0.06 m near the surface and bottom in the shallowest locations to 2.81 m in the center of the domain. The periodic along-shelf direction is 8 km long and the horizontal resolution is 1 km × 1 km for the whole domain.

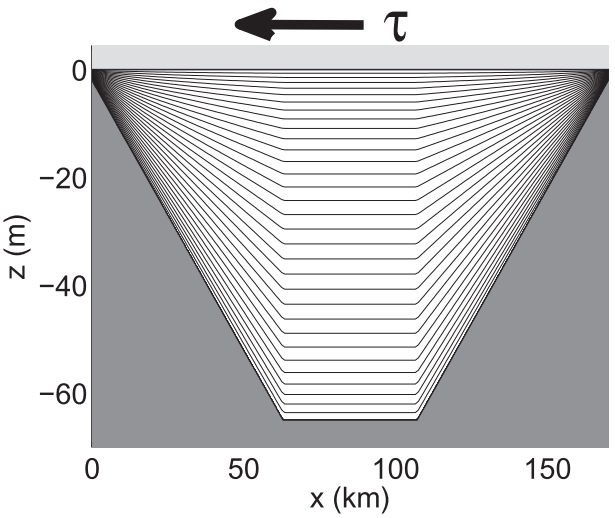

FIG. 2. Cross section of model domain with vertical grid shown in black. Horizontal grid has uniform 1-km spacing. Land is dark gray. Free surface ζ is allowed to vary around $z = 0$ m. Wind stress is applied at free surface.

The model is run with the cross-shelf coordinate positive and increasing to the right as shown in Fig. 2. In all cases the model is forced with a spatially uniform, cross-channel wind stress. The opposite sides of the channel experience opposite wind stresses relative to the coast. Results from a single model run are presented as the two coasts modeled with opposite direction wind forcing. All data analysis in this paper is presented in an ''East Coast,'' right-handed, coordinate system. The cross-shelf coordinate x is zero at the coast and increases offshore. The along-shelf coordinate y is positive in the direction of an upwelling-favorable wind stress.

2) DENSITY

Density varies with a linear equation of state $\rho = \rho(T, S, P)$ for temperature T, salinity S, and pressure P, and all density variation is imposed as changes in temperature. When a surface heat flux is used, it is as a temperature flux through the surface $Q/\rho_o c_p$ (°C m s^{-1}) using a seawater specific heat capacity $c_p = 3985$ J kg^{-1} °C^{-1}.

For model runs with an initial cross-shelf density gradient, isopycnals began uniformly diagonal. The model is initialized with no velocity, but with a surface tilt that opposes the cross-shelf pressure gradient that results from the

initial cross-shelf density gradient. The surface elevation is chosen so $u = 0$ at one-half of the total water depth.

3) MIXING

In ROMS, the system of governing equation is closed by parameterizing Reynolds stresses and turbulent fluxes with eddy viscosities and diffusivities. Eddy viscosity and diffusivity are estimated by the Mellor–Yamada 2.5 (Mellor and Yamada 1982) turbulence closure scheme with the Kantha and Clayson (1994) stability function. The background value of vertical eddy viscosity K_m is $10^{-5}\,\mathrm{m^2\,s^{-1}}$, and the background value of vertical diffusivity for temperature K_C is $10^{-6}\,\mathrm{m^2\,s^{-1}}$. A logarithmic bottom drag coefficient is applied at the center height of each bottom grid cell, which varies in height with the stretched grid. The resulting stress is quadratic with local velocity and scaled by the log of the distance from the apparent bottom roughness $z_0 = 1\,\mathrm{cm}$:

$$\frac{\boldsymbol{\tau}^b}{\rho_o} = C_D \mathbf{u}|\mathbf{u}| \quad \text{with} \quad C_D = \frac{\kappa^2}{\left(\ln \frac{z}{z_0}\right)^2}. \tag{3}$$

b. Base case

The base case run has a bottom slope of $\alpha = 10^{-3}$, for a maximum depth of 65 m and the Coriolis parameter is a constant $f = f_0 = 10^{-4}\,\mathrm{s^{-1}}$. The model is initialized with a constant vertical temperature gradient of $0.25^\circ\mathrm{C\,m^{-1}}$, which creates horizontal isopycnals and an initial stratification of $N^2 = 4.25 \times 10^{-4}\,\mathrm{s^{-2}}$. The cross-shelf wind stress begins at zero and increases over the first two days as $\tau^s(t) = -0.1\sin(\pi t/4)$, where t is time in days. The wind stress is steady over the final three days of model time with $\tau^{sx} = -0.1\,\mathrm{Pa}$ and $\tau^{sy} = 0$. The negative sign of the cross-shelf wind means that the stress is onshore on the left side of the channel and offshore on the right side, as shown in Fig. 2.

c. Model runs

Other model runs start with the base case parameters, initial conditions, and wind forcing, and they typically vary only one of the model parameters. Table 1 summarizes inputs for all model runs used in this paper. Runs used for model testing but not specifically addressed here are also included for completeness. In most analyses, the base case run (top of Table 1) is included and discussed as part of the suite of model runs under investigation. In figures throughout this paper, variables are indicated as the base case (circle), varying wind stress magnitude (triangle), initial stratification (diamond), water depth (asterisk or dot), bottom slope (square), initial cross-shelf density gradient (asterisk), and surface heat flux (plus sign).

Parameters for the base case and model runs with wind stress magnitude, initial stratification, and bottom slope variation were chosen to match those used by Tilburg (2003). For model runs with a surface heat flux, values of Q ($\mathrm{W\,m^{-2}}$) are representative of summertime daily averages of net surface heat flux over the inner shelf off of Martha's Vineyard. For model runs with an initial cross-shelf density gradient, density gradients are representative of summertime near MVCO. Mid-Atlantic Bight climatologies of temperature and salinity (Lentz 2008) and density (Zhang et al. 2011) indicate that uniformly sloped isopycnals are representative of the seasonal mean near Martha's Vineyard. A thermal wind shear is spun up in the first inertial period of the model run.

3. Field data

a. Measurements

Field data for this analysis were generated primarily by the National Science Foundation (NSF)-funded Stratification, Wind, and Waves on the Inner shelf of Martha's Vineyard (SWWIM) study that included mooring and tripod deployments on a cross-shelf transect south of Martha's Vineyard. From October 2006 to February 2010, observations were made at four sites in 7-, 12-, 17.5-, and 27.5-m water depth, located 0.4, 1.5, 3.8, and 11.1 km from shore, respectively (Fig. 3). Velocity and density data from the 12-, 17-, and 27-m sites will be used in this paper.

In 17 and 27 m depth, 600-kHz Teledyne RD Instruments Workhorse Acoustic Doppler Current Profilers (ADCPs) measured velocity in 0.5-m bins from 2.25 meters above the bed (mab), up to 2.75 m below the surface. The ADCPs collected data at 1 Hz for 5 min out of every twenty and recorded only the burst averages while calculating and recording wave spectrum data at 2 Hz for 10 min every four hours.

The MVCO node at 12-m water depth provided velocity, and wave height, direction, and spectrum. The 1200-kHz ADCP there collects 2-Hz velocity data in 0.5-m bins from 2.5 to 10 mab. The MVCO data are provided as 20-min averages and are available online (at www.whoi.edu/mvco/).

Moorings located near the ADCP tripods measured temperature roughly every 2.5 m throughout the water depth with alternating SeaBird MicroCATs and Onset Temp Pros (Fig. 3). The MicroCATs also measured conductivity at their 5-m spacing. The MicroCATs sampled every 1.5 min and the Temp Pros sampled every 10 min. All temperature and conductivity data are averaged and interpolated onto the ADCP 20-min time base.

TABLE 1. Model runs.

Expt	Run	$\lvert\tau^s\rvert$ (Pa)	Initial N^2 ($10^{-4}\,s^{-2}$)	α (10^{-3})	Q ($W\,m^{-2}$)	$\partial\rho/\partial x$* ($10^{-5}\,kg\,m^{-4}$)	f ($10^{-4}\,s^{-1}$)
Base case	1	0.1	4.25	1.0	0	0	1.0
Unstratified Vary τ^x	2	0.01	0	1.0	0	0	1.0
	3	0.013					
	4	0.023					
	5	0.036					
	6	0.05					
	7	0.1					
	8	0.2					
	9	0.36					
Vary τ^x	10	0.01	4.25	1.0	0	0	1.0
	11	0.05					
	12	0.2					
	13	0.36					
Vary N^2	14	0.1	0.0425	1.0	0	0	1.0
	15		0.213				
	16		0.850				
	17		8.50				
	18		10.63				
Vary α	19	0.1	4.25	0.5	0	0	1.0
	20			2.0			
Vary $\partial\rho/\partial x$	21	0.1	1.70	1.0	0	0	1.0
	22					1.75	
	23					3.49	
	24					8.73	
	25					11.64	
	26					17.46	
	27					−1.75	
	28					−3.49	
	29					−8.73	
	30					−11.64	
	31					−17.46	
	32	0	1.70	1.0	0	1.75	1.0
	33					3.49	
	34					8.73	
Vary Q	35	0.1	4.25	1.0	−10	0	1.0
	36				10		
	37				50		
	38				100		
	39				150		
	40				200		
	41	0.05	4.25	1.0	50	0	1.0
	42				150		
Vary f	43	0.1	4.25	1.0	0	0	0.5
	44						1.3

* Opposite coast experiences opposite sign density gradient.

b. Data processing

The goal of the ADCP data processing is to isolate the effect of cross-shelf wind stresses on cross-shelf velocities. First, barotropic tidal currents were estimated for each site using the T_TIDE MATLAB package (Pawlowicz et al. 2002) for tidal constituents with periods less than a month and those predictions were subtracted from the observed current profiles. There is a substantial offshore flow at these sites driven by surface gravity waves (undertow) with a vertical structure that is roughly equal in magnitude but opposite in direction to the Stokes drift velocity (Lentz et al. 2008). Because the surface waves are correlated with the cross-shelf wind stress, we remove this component of the wave-driven flow by adding the Stokes (1847) velocity in the direction of wave propagation, estimated as

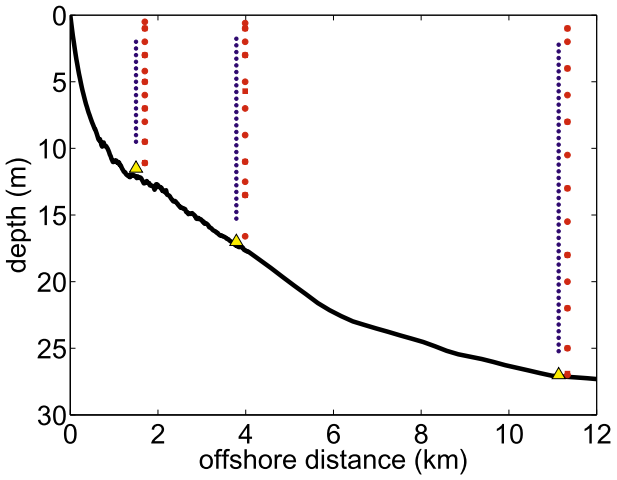

FIG. 3. Cross-shelf bathymetry. Yellow triangles indicate locations of upward-looking ADCPs, blue circles are the locations of ADCP velocity and backscatter measurements, red circles are the locations of temperature measurements, and red squares indicate conductivity and temperature measurements.

$$u_{\mathrm{St}} = \frac{H_{\mathrm{sig}}^2 \omega k}{16} \frac{\cosh[2k(z+h)]}{\sinh^2 kh}, \tag{4}$$

to the observed, detided current profiles at each site. A 24-h half-amplitude filter is applied to depth-averaged velocity before using principal component analysis to define ''along shelf'' as the major axis of velocity variation at each ADCP site. For the 12-, 17-, and 27-m sites, positive along-shelf flows (y axes) are oriented toward 96°, 97°, and 102° clockwise from geographic north.

To estimate the cross-shelf transport, first the ADCP velocity profiles are extrapolated to the surface and bottom. The top three measurements are used to linearly extrapolate velocity to the surface, and the bottom velocity is set to zero. The depth-average of the extrapolated velocity profile is then removed to satisfy the no net cross-shelf transport requirement of the two-dimensional model. Finally, cross-shelf transport in the upper water column is calculated by integrating the profile from the surface to the first zero crossing of the cross-shelf velocity profile.

Wind stress was estimated from the MVCO Air–Sea Interaction Tower (ASIT) wind observations using a bulk formula (Fairall et al. 2003) and rotated into the same coordinate frame as the currents, with along-shelf wind stress oriented toward 97° clockwise from geographic north. Wind stress, currents, and transports were low-pass filtered using a filter with a 24-h half amplitude to focus on subtidal variability.

c. Regressions with forcing terms

A linear regression is used to relate cross-shelf velocity u at each ADCP bin (with depth average removed) to a shear velocity u_*^x from the cross-shelf component of the wind stress τ^{sx}. The regression is a least squares fit to

$$u = a u_*^x + d \quad \text{where} \quad u_*^x = \frac{\tau^{sx}}{|\tau^{sx}|}\sqrt{\frac{|\tau^{sx}|}{\rho_o f}}. \tag{5}$$

With this definition, u_*^x carries the sign of τ^{sx}. The regression coefficient a acts as nondimensional velocity. Profiles of the regression slope represent how cross-shelf circulation responds to cross-shelf wind forcing.

Similarly, a regression is used to relate wind forcing ($u_* h$) to the estimated cross-shelf transport in the upper water column. In this case, the regression takes the form of

$$U = A u_*^x h + D. \tag{6}$$

Regression slope A is the ratio of two values with units of transport, so it represents a nondimensional transport. A multiple regression analysis including cross-shelf wind stress, along-shelf wind stress, and wave forcing yields similar regression coefficients for u_*^x in Eqs. (5) and (6).

4. Inner-shelf circulation

a. Width of inner shelf

Following Tilburg (2003), for a purely cross-shelf wind stress we define the inner shelf as the region onshore of where the surface boundary layer intersects the bottom (e.g., Fig. 6a, described in greater detail below). For a constant bottom slope α, the width of the inner shelf is $(\delta - h_o)/\alpha$, where δ is the thickness of the surface boundary layer. The expression

$$\delta_{N^2} = \frac{0.6 u_*}{f[1 + N^2/(16f)^2]^{1/4}}, \tag{7}$$

where N^2 is the initial stratification, provides an accurate estimate of the surface boundary layer thickness (here, defined as the depth where the streamfunction of the cross-shelf circulation is zero) for both initially stratified and unstratified model runs. [This is a modification of the expression proposed by Tilburg (2003), which provided accurate estimates for stratified runs but not for unstratified runs.] Thus, when stratification is larger, the surface boundary layer is thinner and the inner shelf is narrower.

Stratification also limits the deep-water value that the cross-shelf transport must match at the offshore edge of the inner shelf. In water depths greater than δ_{N^2}, the transport parallel to the wind is sensitive to the vertical mixing, which is affected by both the wind stress magnitude

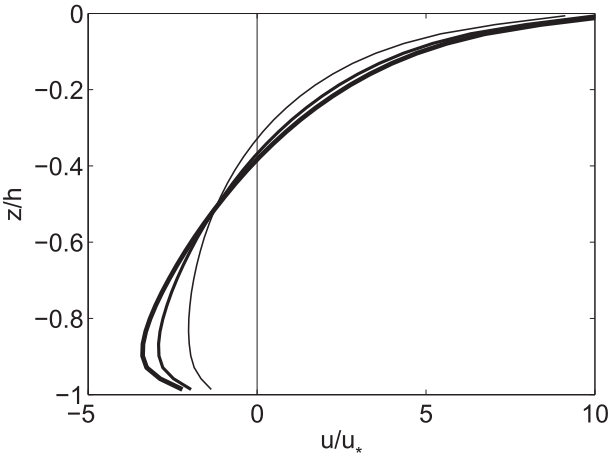

FIG. 4. Nondimensional cross-shelf velocity profiles for unstratified conditions. Profiles are from 10-m water depth and wind stress magnitudes of −0.01 (thinnest line), −0.036, and −0.36 Pa (thickest line), from runs 2, 5, and 9, respectively.

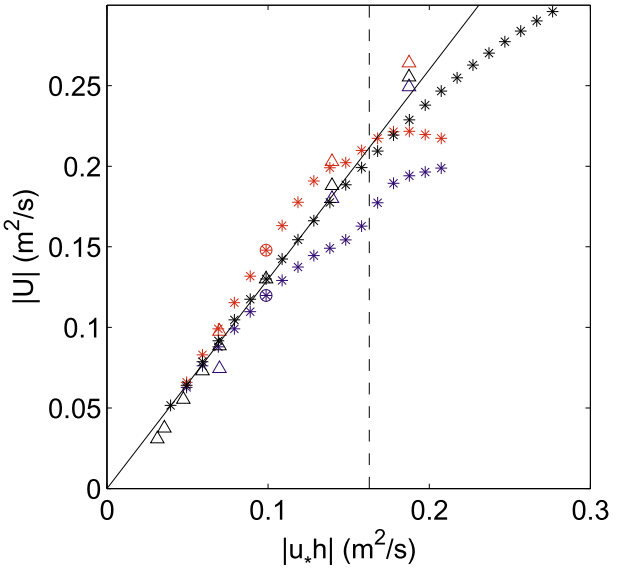

FIG. 5. Cross-shelf transport U compared to expected inner-shelf scaling u_*h at $h = 10$ m for initially stratified runs with on- (blue) and offshore (red) cross-shelf wind stresses of 0.05, 0.1, 0.2, and 0.36 Pa (triangles, with a circle for the base case run) and unstratified (black) runs with wind stresses of 0.01, 0.013, 0.023, 0.036, 0.05, 0.1, 0.2, and 0.36 Pa. Transport is from the base case for $h = 5$–21 m and from the $\tau^x = 0.1$ Pa unstratified case for $h = 4$–28 m (asterisk). Solid line indicates a slope of 1.3. Dashed line indicates $u_*h = 0.16$, the value where $h = \delta_{N^2}$ for the base case run.

and initial stratification (Tilburg 2003). The model runs described in sections 4d and 4e generate transport values from $0.17 \times (\tau^{sx}/\rho_o f)$ to $0.34 \times (\tau^{sx}/\rho_o f)$ at the center of the domain.

While δ_{N^2}/α defines the width, the relevant vertical length scale over the inner shelf is the one that sets the vertical mixing, and subsequently the momentum balance. Because the inner shelf is unstratified (or nearly so, e.g., Fig. 10a, described in greater detail below), the local momentum balance between wind stress and pressure gradient is not affected by the remaining deep stratification far offshore. As a result, δ_{Ek} is the relevant vertical length scale over the inner shelf.

b. Constant density cases

Using the model initialized with a constant density (no vertical or horizontal variation), we identify how the circulation and transport vary with changes in wind stress and water depth. Once the neutral density response is understood, subsequent experiments with initial stratification will be used to isolate the effect of the density field on the inner-shelf response to wind stress.

In constant density conditions, when a cross-shelf wind stress is balanced by a cross-shelf pressure gradient, the circulation is uniform across the inner shelf when depth is scaled by the total water depth. Figure 4 shows profiles from 10-m water depth, for cross-shelf wind stresses of −0.01, −0.036, and −0.36 Pa, yielding shear velocity values $u_* = u_*^x = 0.31, 0.59$, and $1.9\ \mathrm{cm\ s^{-1}}$ and h/δ_{Ek} ratios of 0.13, 0.41, and 0.83, which are all within the inner shelf ($h/\delta_{\mathrm{Ek}} < 1$).

When the wind blows across a constant density (unstratified) shelf, the inner-shelf cross-shelf velocity profiles collapse together when nondimensionalized by shear velocity and water depth, that is, u/u_* is proportional to z/h for a range of wind stresses or water depths (Fig. 4). The small spread in the nondimensionalized current profiles can be explained by an increase in h/δ_{Ek} and a gradual transition from inner to midshelf following a transition from a pressure gradient/wind stress balance to a three-term balance including the Coriolis acceleration. The profile that is least sheared at middepth is from the smallest wind stress (largest h/δ_{Ek}) and the most sheared profile is from the largest wind stress (smallest h/δ_{Ek}). A higher wind stress thickens the boundary layer, moving the transition to midshelf dynamics farther offshore. In Fig. 4, an onshore wind stress is used, but the response is essentially symmetric in unstratified experiments, so the results for an offshore wind stress are nearly identical.

Cross-shelf transport is proportional to u_*h over the inner shelf (black symbols, Fig. 5) for variations in both wind stress and water depth. The transition from inner to midshelf dynamics can be seen more clearly in the cross-shelf transport. When the water depth is less than the deep-water boundary layer scale, that is, $h/\delta_{\mathrm{Ek}} < 1$ or $h/\delta_{N^2} < 1$, which are equivalent for the unstratified case, the transport increases linearly with u_*h at a slope of

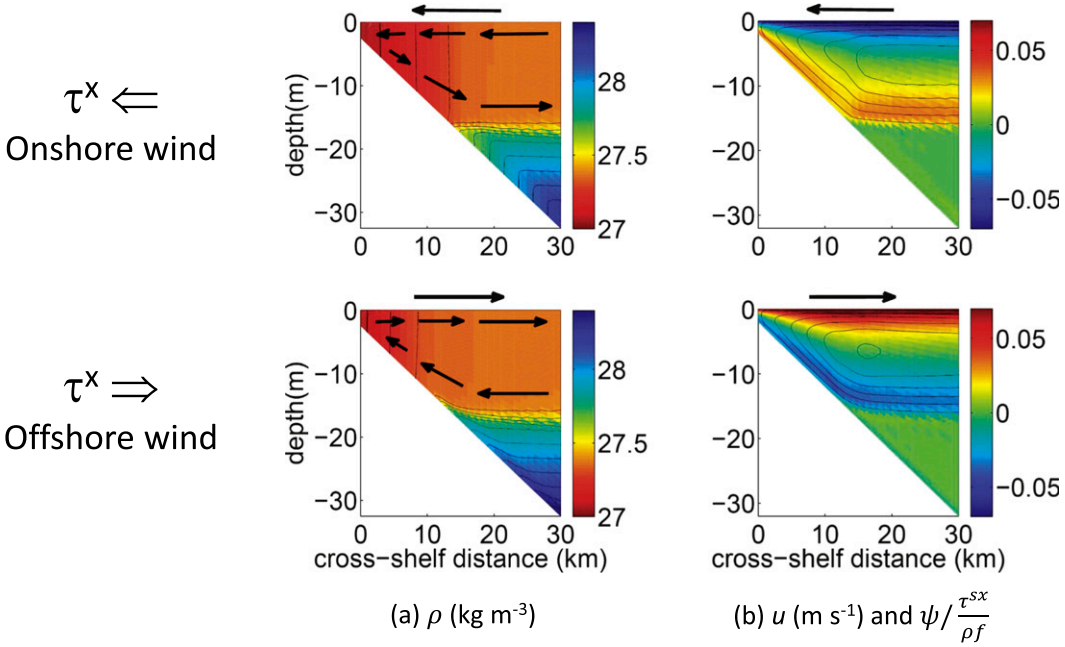

FIG. 6. Inner-shelf fields of (a) density anomaly color and contours (0.1 kg m^{-3} interval), and (b) cross-shelf velocity color and streamfunction contours (0.04 interval), after 5 days of an on- (top) and offshore (bottom) wind stress of 0.1 Pa.

approximately 1.3 (thin black line Fig. 5). The slope is a function of the vertical mixing and the specific shape of the resulting velocity profile. The order-one u/u_* and z/h scalings that seem appropriate for the modeled velocity profiles suggest that the coefficient between U and u_*h should also be order one. As h/δ_{Ek} (or h/δ_{N^2}) approaches one, U approaches a constant. The symbols showing varying water depth can be seen falling away from the 1.3 slope line as h increases. This is in contrast to the symbols showing increasing wind stress, which represent decreasing h/δ_{Ek} values as u_* increases. At mid-shelf, cross-shelf transport reaches a constant value that is proportional to the wind stress and independent of the water depth. The downwind transport in deep water depends on the vertical mixing, in contrast to the cross-wind transport (Tilburg 2003; Fewings et al. 2008; Lentz and Fewings 2012). We find deep-water transport values from $0.35 \times (\tau^{sx}/\rho_o f)$ to $0.38 \times (\tau^{sx}/\rho_o f)$ at the center of the domain when $\kappa u_*/f$ is less than the water depth of 65 m.

c. *Initially stratified "base case"*

When wind blows across an initially stratified shelf, a surface mixed layer develops. For water depths less than the thickness of the surface mixed layer (the inner shelf), a circulation develops that is similar to the unstratified case (cf. Figs. 1 and 6). Both on- (Fig. 6, top) and offshore (Fig. 6, bottom) wind stresses drive near-surface circulation in the direction of the wind stress with a return flow in the lower portion of the water column (Fig. 6b, and indicated by arrows in Fig. 6a). Vertical mixing of the initial stratification over the sloping bottom creates a cross-shelf density gradient on the inner shelf because the bathymetry intersects increasingly dense isopycnals with depth. For all cases with initially horizontal isopycnals, the resulting cross-shelf density gradient is positive regardless of wind direction.

The interaction of the cross-shelf circulation with the cross-shelf density gradient is the primary cause of the difference between the response to on- and offshore wind stresses. An offshore wind stress blows from the less dense nearshore region toward the denser, deeper region of the inner shelf (Fig. 6a, bottom) creating a small positive stratification as a result of buoyancy advection. The stratification reduces vertical mixing and in turn allows greater vertical shear and greater cross-shelf transport. The increased cross-shelf transport across the cross-shelf density gradient feeds back positively on the stratification. The transport does not run away, unbounded, with increasing stratification because the process is still limited by shear instability. For offshore wind (red lines in Fig. 7), both N^2 and Richardson number (Ri) peak where there is near zero shear in the velocity at the height of the peak onshore return flow. The peak Ri is about 0.4 and limits the eddy viscosity to a constant 10^{-4} m^2 s^{-1} in the bottom few meters of the water column while eddy viscosity increases approximately linearly away from the bottom boundary in the neutral case

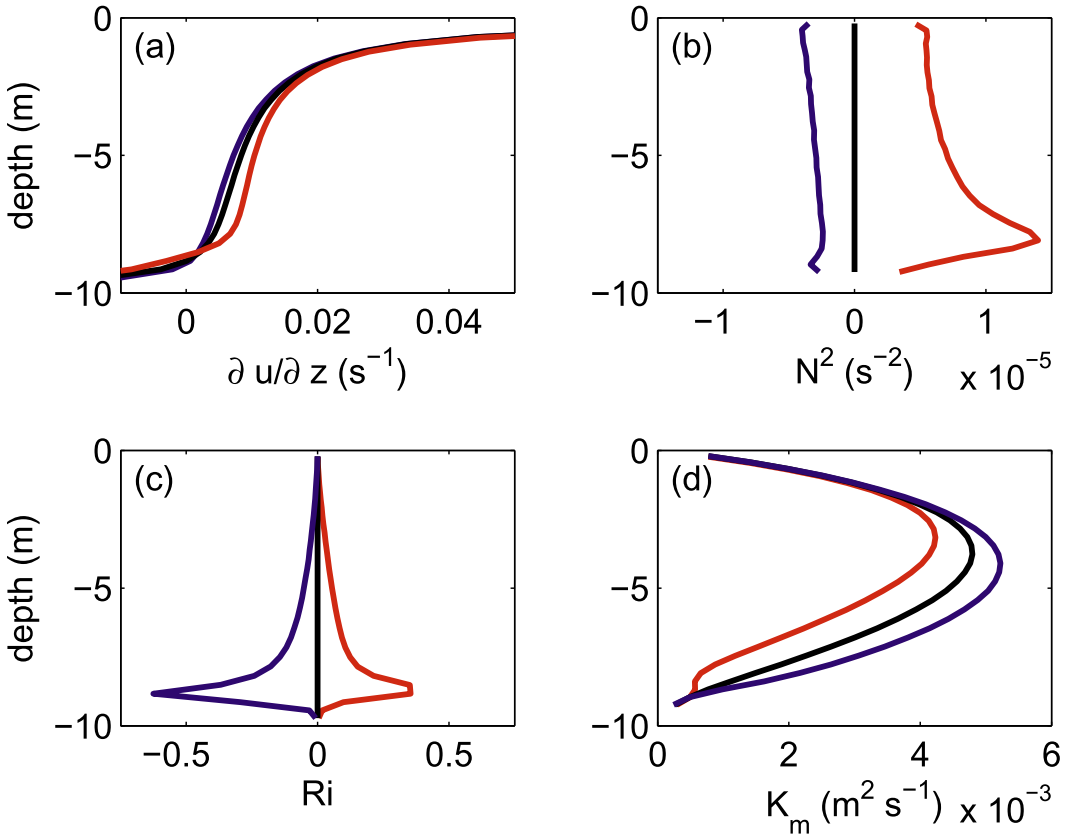

FIG. 7. (a) Shear $\partial u/\partial z$, (b) N^2, (c) Ri $= N^2/(\partial u/\partial z)^2$, and (d) K_m, resulting from on- (blue) and offshore (red) wind stresses in the initially stratified base case (run 1) and onshore wind stress in the constant density model run 7 (black). Shear for onshore winds are shown as $-\partial u/\partial z$ for easier visual comparison to offshore wind.

(black line). The weak positive stratification throughout the water column creates an Ri of 0.05–0.01 throughout most of the water column, causing a decreased eddy viscosity relative to the neutral density case. The resulting slight increase in shear throughout the water column allows a higher cross-shelf transport, which will be quantified in the next several sections.

An onshore wind stress blows from the denser offshore water toward the less dense nearshore water (Fig. 6a, bottom) creating a small negative stratification (Fig. 7b, blue line), which allows greater mixing and so reduces shear and transport. The reduced transport decreases the buoyancy advection that creates the negative stratification and the increased mixing also weakens the negative stratification. Both of these processes bring the density profile closer to neutral. This negative feedback causes the buoyancy advection by onshore winds to have a smaller effect on transport than the opposite direction buoyancy advection by offshore winds. The resulting N^2 and Ri are negative (Figs. 7b,c; blue lines). The negative stratification has the largest magnitude near the surface, but the profile is nearly linear, with no pronounced maximum as for the positive stratification in offshore wind stress case. The negative Richardson number has the largest amplitude at the height of zero shear of the velocity profile, but it is the negative value throughout the water column that causes a higher eddy viscosity over the neutral case. The increased mixing causes lower shear throughout the lower two-thirds of the water column, which causes reduced transport compared to the neutral density and stratified offshore wind stress cases.

Our examination of this base case model run has suggested that differential advection of the cross-shelf density gradient creates a small final vertical density gradient that enhances or reduces the mixing relative to the unstratified value. As a result, an initial stratification increases $U/(u_* h)$ for offshore wind stress and decreases $U/(u_* h)$ for onshore wind stress compared to the uniform density cases.

d. Varying cross-shelf wind stress magnitude

For an initially stratified shelf, varying the wind stress magnitude or water depth affects the cross-shelf transport in the same way as for the unstratified cases (Fig. 5),

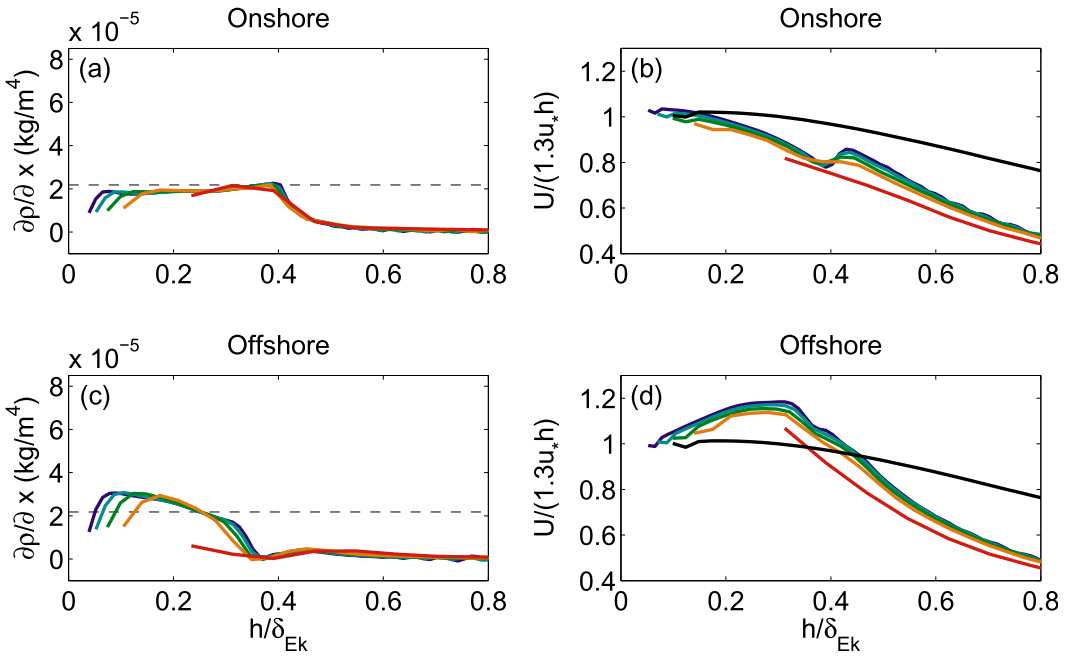

FIG. 8. (a),(c) Cross-shelf density gradient and (b),(d) transport fraction as a function of h relative to the vertical length scale $\delta_{\mathrm{Ek}} = \kappa u_*/f$ generated by on- (top) and offshore (bottom) wind stresses of 0.01, 0.05, 0.1, 0.2, and 0.36 Pa (red, orange, green, teal, and blue lines, respectively) on a shelf initially stratified with $N^2 = 4.25 \times 10^{-4}\,\mathrm{s}^{-2}$. The dashed line in (a) and (c) indicates the cross-shelf density gradient predicted by depth averaging the initial stratification $\partial\overline{\rho}/\partial x = \alpha N_0^2 \rho_0/2g$. An unstratified run (black) with 0.1 Pa wind stress is shown with the stratified results in (b) and (d).

where U increases with u_*h at a slope of approximately 1.3. However, offshore wind stress (red) generates a slightly larger transport than onshore (blue) for given values of u_* and h. In Fig. 5, the bumps up in the blue line of asterisks and down in the red line are near the offshore edge of the inner shelf, where $h = \delta_{N^2}$ (vertical dashed line). At that point, transport by both on- and offshore wind stress transitions to the deep-water value because the surface boundary layer separates from the bottom. In contrast to the unstratified case where the inner- to midshelf transition is smooth, for initially stratified cases, the abrupt transition of the transport scale from u_*h to $\tau/\rho_o f$ occurs where $h = \delta_{N^2}$, which will be at the h/δ_{Ek} value given by $\delta_{N^2}/\delta_{\mathrm{Ek}}$.

To isolate the effect of the density field on the transport from the effects of water depth and wind stress, we compute a nondimensional transport fraction $U/(1.3u_*h)$ as the ratio of the modeled transport to what would be expected in a neutral density case (Fig. 5, black line). The cross-shelf density gradient (Figs. 8a,c) and transport fraction (Figs. 8b,d) are shown as a function of vertical length scale h/δ_{Ek} for on- and offshore wind stresses of varying magnitudes. For both directions of wind stress, the inner- to midshelf transition occurs near $h = \delta_{N^2} = 0.4\delta_{\mathrm{Ek}}$ for the base case initial stratification used in these model runs [Eq. (7)].

For onshore wind stress (Fig. 8, top), the cross-shelf density gradient is constant across the inner shelf and the gradient is well predicted by depth averaging the initial stratification over sloping bathymetry $\partial\overline{\rho}/\partial x = \alpha N_0^2 \rho_o/2g$ (dashed line in Fig. 8a, also see section 5). The transport fractions all collapse together. They are approximately one for small h/δ_{Ek}, then decrease across the inner shelf, with a widening gap between the stratified runs and the unstratified case (included for comparison). At the offshore edge of the inner shelf, where the surface boundary layer has separated from the bottom, the depth continues to increase while the surface density and transport are constant, so the density gradients fall to zero and the transport fractions are proportional to $1/h$.

For offshore wind stress (Fig. 8, bottom), upwelled water makes the outer edge of the inner shelf denser than for onshore wind stress (as can be seen in Fig. 6a), creating a higher cross-shelf density gradient near the coast. The density gradient decreases with distance from the coast over the inner shelf, in contrast to the runs for onshore wind stress. The transport fractions all fall together, increasing across the inner shelf, with a widening gap between the stratified runs and the unstratified case. As for the onshore wind, where water depth is greater than the surface boundary layer thickness, the

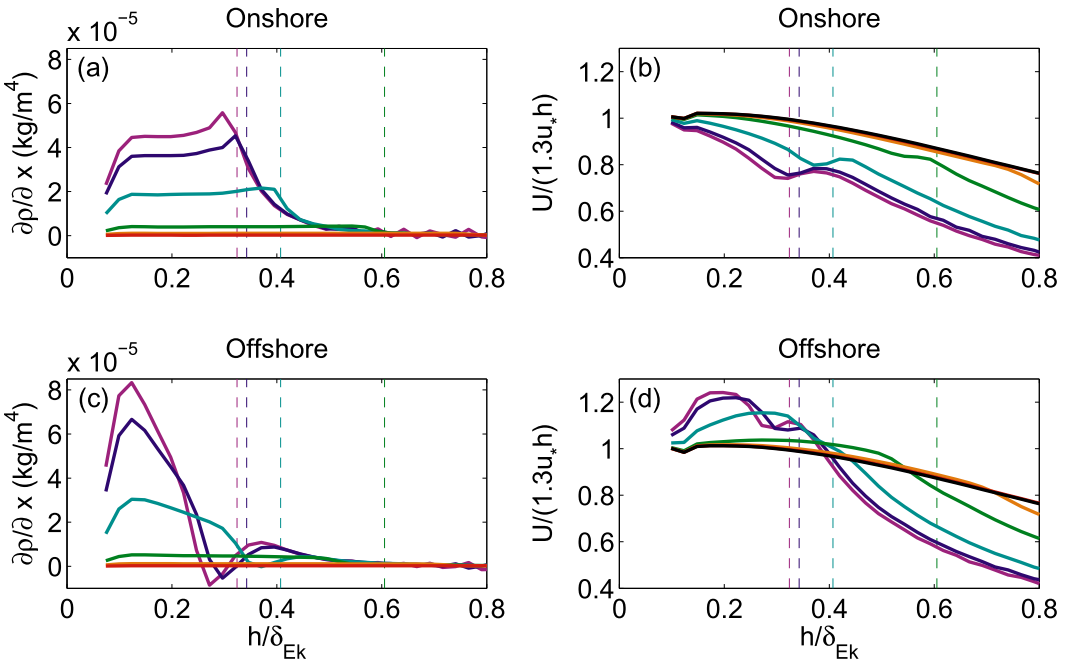

FIG. 9. (a),(c) Cross-shelf density gradient and (b),(d) transport fraction as a function of h relative to $\delta_{\mathrm{Ek}} = \kappa u_*/f$ generated by on- (top) and offshore (bottom) 0.1 Pa wind stress over initial stratification of $N^2 = (0.0425, 0.2125, 0.85, 4.25, 8.5, \text{and } 10.625) \times 10^{-4}\,\mathrm{s}^{-2}$ (red, orange, green, teal, blue, and purple lines, respectively). Dashed lines mark $h = \delta_{N^2}$ for runs where this occurs within our x-axis limits, indicating where the water depth becomes greater than the surface boundary layer thickness. An unstratified run (black) with 0.1 Pa wind stress is shown with the stratified results in (b) and (d) and largely obscures the red line.

cross-shelf density gradients fall to zero and the transport fractions are proportional to $1/h$.

e. *Varying initial stratification*

The strength of the initial stratification affects the inner shelf in two ways: it increases the cross-shelf density gradient generated by vertical mixing over sloping bathymetry and it limits the deep-water boundary layer thickness (δ_{N^2}). The cross-shelf density gradient affects the transport on the inner shelf, while the boundary layer thickness sets the width of the inner shelf. Figure 9 shows the cross-shelf density gradient and transport fraction for on- and offshore wind stresses for six different initial stratifications. For each model run, the edge of the inner shelf at $h = \delta_{N^2}$ is indicated by a dashed line at the corresponding h/δ_{Ek} value, which ranges from 0.32 to 1.15. The inner- to midshelf transition occurs near $h = \delta_{N^2}$ demonstrating that δ_{N^2}/α is the correct scale for the width of the inner shelf. However, when h is less than δ_{N^2}, it is h/δ_{Ek} that sets the place in parameter space that tells us how important the Coriolis acceleration is relative to vertical mixing. If these data were plotted as a function of h/δ_{N^2} instead of h/δ_{Ek}, the too-small vertical length scale would cause transport for both on- and offshore wind stresses to appear larger for the stratified cases than the constant density case, hiding the result that a negative final stratification should decrease transport.

For onshore wind stress (Fig. 9a), higher initial stratification increases the cross-shelf density gradient uniformly across the width of the inner shelf. The higher cross-shelf density gradient allows a larger (more negative) unstable stratification to be produced over the inner shelf by the wind-driven advection (Fig. 10a, blue symbols). Consequently, increasing initial stratification results in reduced transport fraction over the inner shelf (Fig. 9b and Fig. 10b, blue symbols). Note that the magnitude of the unstable stratification over the inner shelf is 100 times smaller than the initial stratification.

For offshore wind stress, the cross-shelf density gradient (Fig. 9c) increases with increasing initial stratification, but the density gradient is not uniform across the inner shelf. The maximum $\partial\rho/\partial x$, located just a few kilometers from shore, is larger than that predicted purely by vertical mixing of initial stratification. (See values generated by onshore wind stress in Fig. 9a for comparison.) The wind-driven circulation acting on the larger cross-shelf density gradient creates a stronger inner-shelf stratification. Thus, for offshore wind stress, stronger initial stratification results in stronger inner-shelf stratification

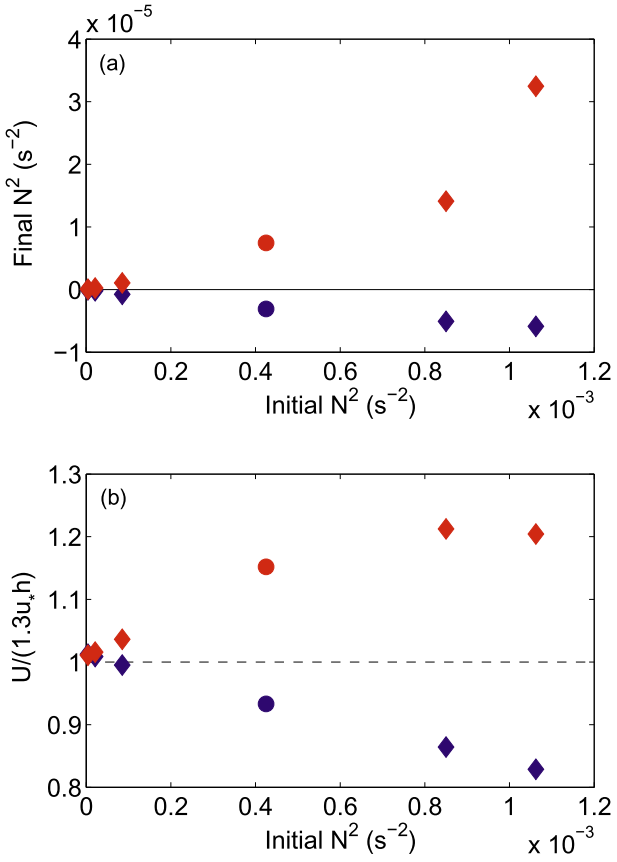

FIG. 10. (a) Final stratification and (b) transport fraction as a function of initial stratification (diamonds, with a circle for base case run) at 10-m water depth for on- (blue) or offshore (red) cross-shelf wind stresses of 0.1 Pa.

(Fig. 10a, red symbols). As noted for onshore wind stresses, the inner-shelf stratification is two orders of magnitude smaller than the initial stratification. The stronger stratification over the inner shelf allows a greater shear and transport to be maintained before the positive feedback process is limited by mixing. Consequently, the inner-shelf transport fraction (Fig. 9d) increases with stronger initial stratification (red symbols in Fig. 10b).

5. Predicting the cross-shelf density gradient

Results from the previous section indicate that the cross-shelf density gradient is a key component in setting the balance between circulation and mixing. Here, we show that a simple one-dimensional model provides accurate estimates of the cross-shelf density gradient over the inner shelf for uniform initial stratification (Table 1, runs 1 and 10–20), as well as for model experiments adding a constant surface heat flux (runs 35–40) or an initial positive or negative cross-shelf density gradient (runs 21–31).

Complete vertical mixing of spatially uniform vertical and horizontal density gradients over a sloping bottom, with no horizontal advection of buoyancy, will generate a cross-shelf density gradient that is the sum of the contributions from the initial stratification $(\cdot)_{N^2}$ and the initial $(\cdot)_0$ horizontal density gradient:

$$\frac{\partial \rho}{\partial x} = \left(\frac{\partial \rho}{\partial x}\right)_{N^2} + \left(\frac{\partial \rho}{\partial x}\right)_0 = -\frac{\alpha}{2}\frac{\partial \rho}{\partial z}\bigg|_0 + \frac{\partial \rho}{\partial x}\bigg|_0. \tag{8}$$

When a spatially uniform surface heat flux is imposed with no advection, after some time, the depth-averaged temperature $\overline{T}$ will have increased over the initial temperature at that location. The corresponding change in density is proportional to $\alpha_T Qt/h\rho_o c_p$, where α_T is the thermal expansion coefficient in the linear equation of state. The cross-shelf density gradient generated by the surface heat flux $(\cdot)_Q$ is given by

$$\left(\frac{\partial \rho}{\partial x}\right)_Q = -\rho_o \alpha_T \frac{\partial \overline{T}}{\partial x} = \rho_o \alpha_T \frac{Qt}{\rho_o c_p}\left(\frac{\alpha}{h^2}\right). \tag{9}$$

The total cross-shelf density gradient due to vertical mixing of initial stratification, surface heat flux, and an initial horizontal density gradient will be

$$\frac{\partial \rho}{\partial x} = \left(\frac{\partial \rho}{\partial x}\right)_{N^2} + \left(\frac{\partial \rho}{\partial x}\right)_Q + \left(\frac{\partial \rho}{\partial x}\right)_0 = -\frac{\alpha}{2}\frac{\partial \rho}{\partial z}\bigg|_0 + \rho_o \alpha_T \frac{Qt}{\rho_o c_p}\left(\frac{\alpha}{h^2}\right) + \frac{\partial \rho}{\partial x}\bigg|_0. \tag{10}$$

Inner-shelf cross-shelf density gradients (Fig. 11a) match the prediction from Eq. (10) for most of the model runs, regardless of whether the density gradient was initially imposed or created by mixing of initial stratification or surface heat flux. However, there are small differences between model and prediction for a few of the model runs (Fig. 11b) when buoyancy advection over the inner shelf is significant. The cross-shelf density gradients plotted in Figs. 8a, 8c, 9a, and 9c showed that offshore wind stress creates variation in the cross-shelf density gradient across the inner shelf, while the onshore wind stress creates a nearly constant density gradient. Correspondingly, the offshore wind (red) data in this subset (Fig. 11b) show a greater spread than the onshore wind (blue) data. In the model runs, advection is most important in modifying the horizontal density structure for offshore wind stress, particularly near the outer edge of the inner shelf. Overall, the close match of $\partial\rho/\partial x$ with Eq. (10) indicates that the cross-shelf density gradient is set primarily by one-dimensional processes (vertical mixing) on the inner shelf in this 2D model.

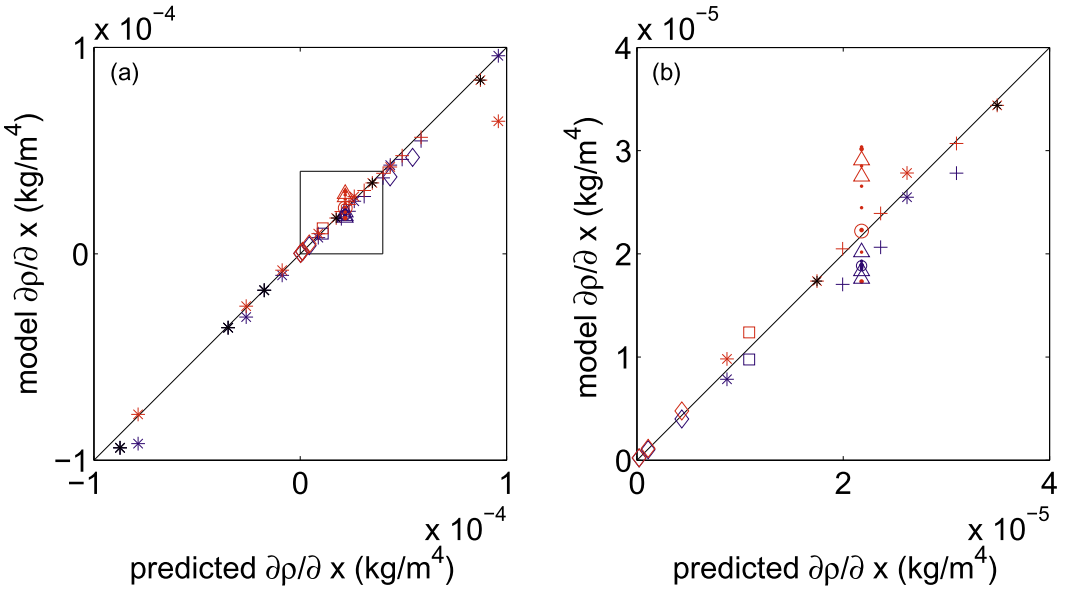

FIG. 11. (a) The $\partial\rho/\partial x$ from the model using ρ from the surface at 10-m water depth (8 km from shore) compared to $\partial\rho/\partial x$ predicted by purely vertical mixing of initial isopycnals. Base case run (circle) and runs varying N_0^2 (diamonds), τ^{sx} (triangles), α (squares), depth (dots), surface heat flux (plus signs) and initial cross-shelf density gradient (asterisks) with onshore (blue), offshore (red), or zero (black) wind stress. (b) Expanded axes for area indicated by box in (a).

6. Effect of the cross-shelf density gradient on cross-shelf transport

As discussed in section 4, a cross-shelf density gradient modifies the wind-driven transport by changing the values of shear and stratification that control vertical mixing and close the governing equations. To quantify the relationship between transport fraction and the horizontal density gradient, we look for the relevant scales to characterize the influence of the cross-shelf density gradient on vertical mixing.

Stratification is created by wind-driven advection of the cross-shelf density gradient. This horizontal buoyancy flux is given by the product of the horizontal buoyancy gradient and the transport scale (Simpson et al. 1990):

$$B_h = \left(\frac{g}{\rho_o}\frac{\partial\rho}{\partial x}\right)u_* h. \tag{11}$$

The buoyancy flux is positive when density increases in the direction of the (near surface) transport and is negative when the density decreases in the direction of transport. The vertical mixing that reduces stratification is generated by shear production of turbulence, which is proportional to the shear scale u_*/h times the stress scale $\overline{u'w'} \sim u_*^2$ giving

$$P = \frac{u_*^3}{h}. \tag{12}$$

The relative strengths of the buoyant suppression (or production) and shear production of turbulence are represented by a horizontal Richardson number (Stacey et al. 2001; Stacey and Ralston 2005):

$$\mathrm{Ri}_x = \frac{B_h}{P} = \frac{g}{\rho_o}\frac{\partial\rho}{\partial x}\frac{h^2}{u_*^2}. \tag{13}$$

This nondimensional number is also called the Simpson number (Simpson et al. 1990), which in estuarine contexts is used to describe the ratio of the buoyancy flux by gravitationally driven estuarine circulation to turbulence generated by tidal stresses rather than the wind-driven advection and mixing that occur on the inner shelf.

Recalling the definition $u_*^2 = \tau^{sx}/\rho_o$, the formula can be rewritten in a way to make clear that this Ri_x is a signed value:

$$\mathrm{Ri}_x = \frac{gh^2}{\tau^{sx}}\frac{\partial\rho}{\partial x}. \tag{14}$$

The Ri_x is positive when wind-driven advection will create positive stratification that limits mixing. Momentum from the wind will be confined nearer to the surface, leading to increased transport in the upper portion of the water column. The Ri_x is negative when the advection will create negative stratification that enhances mixing. Mixing moves high-momentum surface water downward, where it combines with water moving

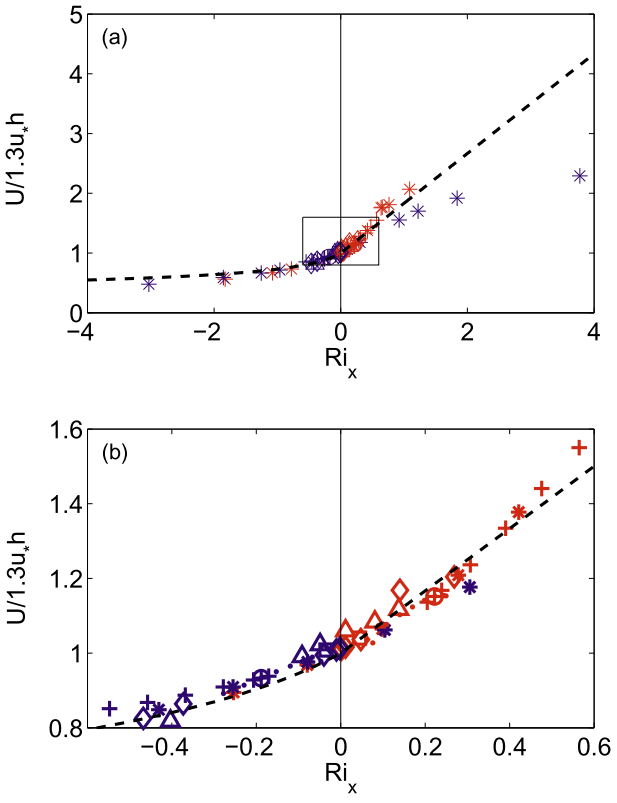

FIG. 12. (a) Model output transport fraction $U/(1.3u_*h)$ compared to the sign of the wind stress times Ri_x for model final $\partial\rho/\partial x$ at 10-m water depth. Color indicates an on- (blue) or offshore (red) wind stress, and the experiment variable is indicated by the symbol: base case (circle), 5–12-m water depth (dots), wind stress magnitude (triangles), initial stratification (diamonds), initial cross-shelf density gradient (asterisks), bottom slope α (squares), and surface heat flux (plus signs). Prediction by Monin–Obukhov similarity theory (black dashed line) shown for comparison. (b) Expanded axes for area indicated by box in (a).

the opposite direction from the lower portion of the water column. Velocities in both the upper and lower portions of the water columns are reduced, so the resulting transport is smaller.

Transport fractions at 10-m water depth plotted as a function of the horizontal Richardson number for all the model runs tend to collapse onto a single curve (Fig. 12). The collapse of all the model runs onto a single curve supports the idea that Ri_x is the key nondimensional number characterizing the inner-shelf response to stratification, surface heat flux, and cross-shelf density gradients. For density values increasing in the direction of the wind stress ($\mathrm{Ri}_x > 0$), an increased density gradient increases transport by increasing stratification and reducing mixing. For a wind stress opposing the density gradient ($\mathrm{Ri}_x < 0$), a larger cross-shelf density gradient decreases the transport fraction by creating negative stratification and more mixing for a particular wind stress magnitude. The steeper slope of the transport for positive Ri_x values than negative ones indicates the transport's stronger response to wind blowing with a given cross-shelf density gradient (from lighter toward denser water) than against it. The larger change in transport for off- than onshore wind stresses shown in section 4e was not just an effect of the higher nearshore density gradient created by offshore wind stresses, but an effect of the two directions of wind stress acting in different ways on the cross-shelf density gradient. By using both positive and negative density gradients with both positive and negative wind stresses, we ensure the asymmetry observed is a true response to Ri_x and not an artifact of each sign of Ri_x only being generated by transport toward shallower or deeper regions. Comparison of transport fraction to horizontal Richardson number at a fixed h/δ_{Ek} value, to ensure the effect of Ri_x on transport fraction is fully isolated, yields a result very similar to the one shown in Fig. 12.

The dependence in Fig. 12, with a larger slope for positive Ri_x, and smaller slope for negative Ri_x, is similar to the response of wind shear to vertical flux Richardson number R_f as described by Monin and Obukhov (1954) similarity theory and demonstrated with atmospheric field measurements by Businger et al. (1971). Monin–Obukhov similarity theory predicts that the nondimensional wind shear in the atmospheric boundary layer will be a function of $R_f = z/L$, where $L = u_*^3/(\kappa B_z)$ is the Monin–Obukhov length scale, with B_z the vertical buoyancy flux from surface heating (e.g., Kundu and Cohen 2004, pp. 566–567; Foken 2006).

While the source of stable or unstable stratification over the inner shelf is not the same as for a one-dimensional atmospheric boundary layer, the basic premise of positive or negative stratification enhancing or suppressing turbulence and, in turn, affecting vertical shear is similar. To compactly summarize our results, we modified the empirical relationship developed by Businger et al. (1971) by including a single-scale factor $c = 1/6$ to fit the observed relationship between Ri_x and normalized transport in Fig. 12,

$$\frac{U}{1.3u_*h} = \begin{cases} (1-\gamma c\mathrm{Ri}_x)^{-1/4} & \mathrm{Ri}_x < 0 \\ (1+\beta c\mathrm{Ri}_x) & \mathrm{Ri}_x \geq 0 \end{cases}, \qquad (15)$$

where we have taken $\gamma = 15$ and $\beta = 5$ following Garrat (1992) (dashed line, Fig. 12). This relationship analogous to Monin–Obukhov similarity theory provides an accurate representation of the model result dependence for $\mathrm{Ri}_x < 1$.

7. Comparison to field observations

Our modeling results indicate the importance of the cross-shelf density gradient in controlling the efficiency

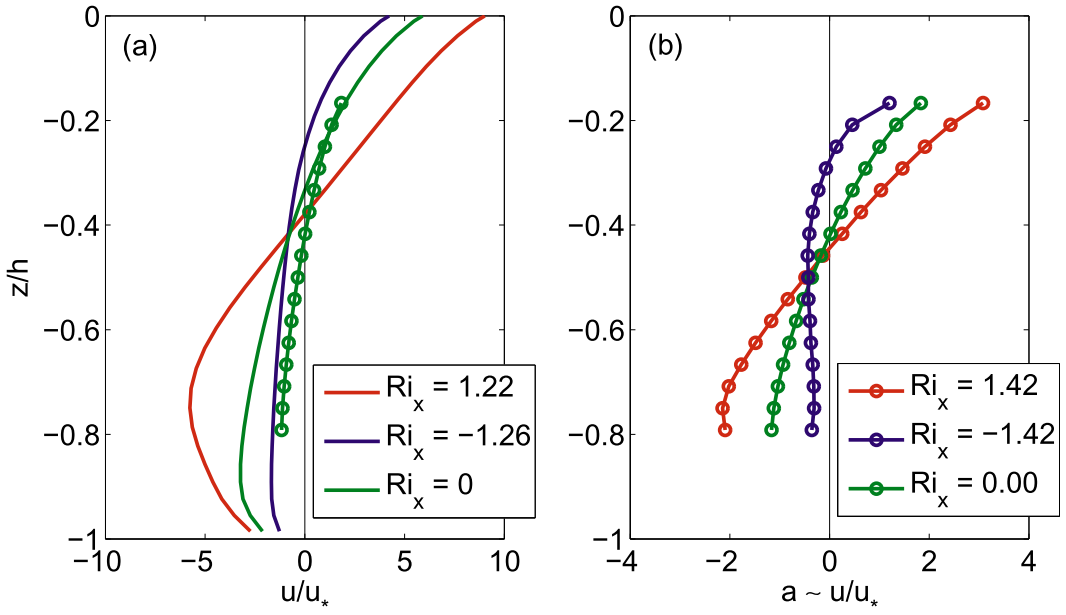

FIG. 13. Profiles of u/u_* from (a) model and (b) SWWIM data. Model profiles at 10-m water depth were chosen from individual runs that generated appropriate Ri_x values. Runs with -0.1 Pa wind stress and initial cross-shelf density gradients of -11.64×10^{-5}, $+11.64 \times 10^{-5}$, and 0 kg m^{-4} and initial stratifications of 1.7×10^{-4}, 1.7×10^{-4}, and 0 s^{-2} are shown in red, blue, and green, respectively. SWWIM profiles from the 12-m site show linear regression coefficients $a \sim u/u_*$ from Eq. (5) applied to data binned in ranges of $-2 < \mathrm{Ri}_x < -1$, $-1 < \mathrm{Ri}_x < 1$, and $1 < \mathrm{Ri}_x < 2$ from times when the 27 m was unstratified (near-surface to near-bottom density difference of less than 0.05 kg m^{-3}). Median Ri_x values given in the legend.

of the cross-shelf wind stress at driving cross-shelf transport. We use measurements from the inner shelf south of Martha's Vineyard to test if the same relationship seen in Fig. 12 and summarized in Eq. (15) is demonstrated by field observations. To ensure that we only consider times when the moored array is on the inner shelf, we limit the analysis to times when density is well mixed at the 27-m site (near-surface to near-bottom density difference less than 0.05 kg m^{-3}) so that $\delta_{N^2} > 27$ m. The cross-shelf density gradient is calculated from the depth-averaged density measurements at the 12- and 27-m moorings, separation 9.6 km. Then Ri_x is estimated using the cross-shelf density gradient, shear velocity from cross-shelf wind stress at the MVCO ASIT in 15-m water depth, and the water depth of each observation site. Cross-shelf velocity and transport estimates from the 12-, 17-, and 27-m sites are regressed (as described in section 3c) against shear velocity and then examined for different range bins of Ri_x.

a. Velocity profiles

Cross-shelf current profiles driven by cross-shelf wind stress from the model and observations exhibit a similar vertical structure and dependence on Ri_x (Fig. 13). Velocity profiles from the model (solid) and regression slope profiles from observations (circles) both show larger magnitude and middepth shear for positive Ri_x and a lower magnitude and middepth shear for a negative Ri_x relative to the zero Ri_x profiles.

The normalized currents u/u_* from the model have larger magnitudes than from the observations. This difference is consistent with our understanding that, at this field site, tidal velocities are large (0.3 m s^{-1}) and the resulting mixing will reduce shear in the observed velocity profiles. Any along-shelf component of the wind stress would also contribute to mixing. By comparison, Lentz and Fewings (2012) found a closer match between modeled and measured profile magnitudes on the North Carolina inner shelf, where tides are weak. This effect of tides reducing wind-driven circulation on the inner shelf was demonstrated numerically by Castelao et al. (2010) for upwelling wind stresses.

b. Cross-shelf transport

The dependence of transport fraction estimates from the 12- (blue symbols, Fig. 14), 17- (red), and 27-m (cyan) sites on Ri_x is similar to the model dependence (Fig. 12) and both follow the curve predicted by Monin–Obukhov similarity theory (black dashed line). As with the model output, the observations are normalized to make the transport fraction one when Ri_x is zero. The regression slope A_0 between transport U and transport

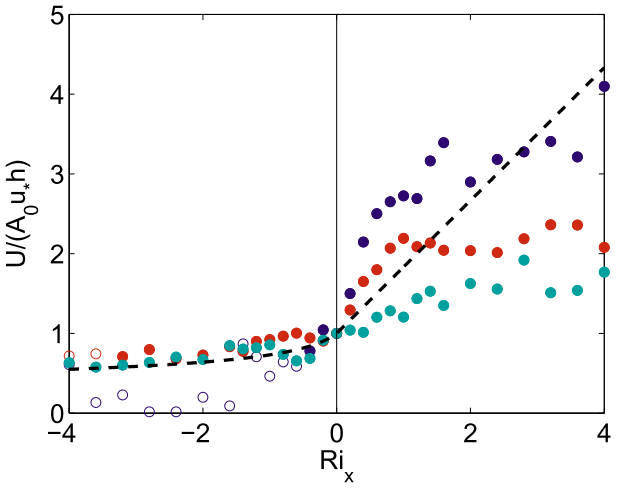

FIG. 14. Transport fraction as a function of Ri_x from SWWIM data from 12- (blue, $A_0 = 0.17$), 17- (red, $A_0 = 0.22$), and 27-m (cyan, $A_0 = 0.26$) sites. Transport fraction is given by regression coefficient $A \sim U/u_*h$ from Eq. (6) as applied to data binned by Ri_x in 0.2 increments from times when the 27-m was unstratified (near-surface to near-bottom density difference of less than 0.05 kg m^{-3}). Open symbols indicate a correlation coefficient less than 0.3. Prediction by Monin–Obukhov similarity theory (black dashed line) shown for comparison.

scale u_*h found for neutral-density conditions is lower for all three field sites than for the model results. As with the velocity regressions, this difference is likely due to large tidal velocities causing mixing at Martha's Vineyard, but not in the model. The regression increases with water depth across the three sites, possibly a result of less tidal mixing at the larger water depths.

At all three sites, the observations show a reduced transport fraction for $Ri_x < 0$ and enhanced transport fraction for $Ri_x > 0$ relative to the transport fraction for $Ri_x = 0$. For $|Ri_x|$ less than one, the data show a higher slope for positive Ri_x than for negative Ri_x, consistent with model results. Transport fraction at the 12-m site shows the strongest response (larger change from $U/A_0u_*h = 1$) to the horizontal Richardson number and the 27-m site shows the weakest. Part of this difference may be a result of using a single estimate of the cross-shelf density gradient for the three sites, while knowing that the gradient is likely stronger closer to shore, as is expected over the steeper bathymetry near shore (Fig. 3), and indicated by sparser and noisier density measurements collected at 7-, 15-, and 17-m water depths. Using too large a value of $\partial\rho/\partial x$ for the 27-m site would place points at too large a value of Ri_x, making the effect of Ri_x on transport fraction appear weaker. Conversely, the response may appear too strong for the 12-m site if the cross-shelf density gradient has been underestimated.

For Ri_x greater than one, the data (Fig. 14) and limited model runs (Fig. 12) show that the transport fraction appears to change less rapidly in response to further increases in Ri_x than for Ri_x less than one. When Ri_x is small, the wind stress term is much larger than the baroclinic pressure gradient term in the cross-shelf momentum balance. In these cases, the cross-shelf density gradient affects the circulation by how it alters the vertical mixing, but does not directly drive the flow. For larger Ri_x, the baroclinic pressure gradient term is similar in magnitude to the wind stress and the two terms are equal in magnitude when Ri_x equals two. When the baroclinic pressure gradient is a significant term in the momentum equation, the cross-shelf density gradient will directly drive circulation in addition to its effect on the vertical mixing; in this case the system is in a different dynamical regime from the one Monin–Obukhov theory explains and it is not surprising our model and observations diverge from the empirical relationship [Eq. (15)].

8. Conclusions

This paper was motivated by field observations and previous modeling work that left open the question: how does cross-shelf wind stress drive circulation on an initially stratified inner shelf? How does the density field affect the circulation and why is the response to on- and offshore wind stresses asymmetric? We use an idealized, 2D, cross-shelf transect in ROMS to describe the effects of initial stratification, wind stress magnitude, surface heat flux, and cross-shelf density gradient on the inner-shelf response to cross-shelf wind stress. To first order, the cross-shelf transport U scales like u_*h, but the transport fraction U/u_*h does depend on the density field and h/δ_{Ek}.

Over sloping bathymetry, vertical mixing of initial stratification or a surface heat flux creates a cross-shelf density gradient. Under cross-shelf wind stresses, the resulting cross-shelf gradient for water depths less than the deep-water boundary layer thickness is well represented by a prediction based on complete vertical mixing of all contributions to the density field [Eq. (10)]. Straining of the resulting cross-shelf density gradient increases transport by offshore winds and decreases transport by onshore winds, but does not generate a strongly stratified inner shelf for either wind direction. For a positive cross-shelf density gradient (lighter water near the coast), an offshore wind stress moves lighter over denser water, creating a small positive stratification, which allows increased vertical shear in the cross-shelf velocity profile and increased transport. The increased transport feeds back positively on the increased stratification

until the process is limited by shear instability. An onshore wind stress moves denser over lighter water, creating a small negative stratification, which increases mixing and decreases transport. The decreased transport reduces the buoyancy advection that creates the negative stratification and the increased mixing also destroys the negative stratification, so the process that alters transport by onshore wind stress is more self-limiting than that for offshore wind stress.

The horizontal Richardson number is the scale for the cross-shelf density gradient. Transport fraction is a function of Ri_x and the relationship collapses for all model runs. Figure 12 demonstrates the empirical relationship [Eq. (15)] between the cross-shelf density gradient and the efficiency of the cross-shelf wind at driving transport.

This result is particularly important for planning field investigations and interpreting data because the cross-shelf density gradients analyzed here, along with wind stresses and water depths, are measurable with common observational techniques. In contrast, the small stratification resulting from horizontal buoyancy advection across the inner shelf, as described in sections 4c–e and shown in Fig. 10a are not readily measurable from the SWWIM dataset or from other similar moored observations. Observations from the inner shelf south of Martha's Vineyard support the modeling results. The similar results for model and field observations in Figs. 12 and 14 provide compelling evidence that it is the cross-shelf rather than vertical density gradient that is critical to predicting transport driven by a cross-shelf wind stress.

Acknowledgments. This work was funded by Ocean Sciences Division of the National Science Foundation Grant OCE-0548961 and by the Woods Hole Oceanographic Institution through the Academic Programs Office and the Coastal Ocean Institute. Data central to this study were provided by the Martha's Vineyard Coastal Observatory, which is funded by WHOI and the Jewett/EDUC/Harrison Foundation. Thanks to Craig Marquette, Captain Ken Houtler, and crew member Ian Hanley of R/V *Tioga* for instrument assembly, deployment, and recovery and thanks to Rocky Geyer for suggesting investigating the Monin–Obukhov comparison.

REFERENCES

Austin, J. A., and S. J. Lentz, 2002: The inner shelf response to wind-driven upwelling and downwelling. *J. Phys. Oceanogr.,* **32,** 2171–2193.

Businger, J. A., J. C. Wyngaard, Y. Izumi, and E. F. Bradley, 1971: Flux-profile relationships in the atmospheric surface layer. *J. Atmos. Sci.,* **28,** 181–189.

Castelao, R., R. Chant, S. Glenn, and O. Schofield, 2010: The effects of tides and oscillatory winds on the subtidal inner-shelf cross-shelf circulation. *J. Phys. Oceanogr.,* **40,** 775–788.

Cudaback, C. N., L. Washburn, and E. Dever, 2005: Subtidal inner-shelf circulation near Point Conception, California. *J. Geophys. Res.,* **110,** C10007, doi:10.1029/2004JC002608.

Dzwonkowski, B., K. Park, and L. Jiang, 2011: Subtidal across-shelf velocity structure and surface transport effectiveness on the Alabama shelf of the northeastern Gulf of Mexico. *J. Geophys. Res.,* **116,** C10012, doi:10.1029/2011JC007188.

Ekman, V. W., 1905: On the influence of the earth's rotation on ocean currents. *Arkiv Math. Astro. Fys.,* **2,** 1–53.

Estrade, P., P. Marchesiello, A. C. De Verdiere, and C. Roy, 2008: Cross-shelf structure of coastal upwelling: A two dimensional extension of Ekman's theory and a mechanism for inner shelf upwelling shut down. *J. Mar. Res.,* **66,** 589–616, doi:10.1357/002224008787536790.

Fairall, C. W., E. F. Bradley, J. E. Hare, A. A. Grachev, and J. B. Edson, 2003: Bulk parameterization of air–sea fluxes: Updates and verification for the COARE algorithm. *J. Climate,* **16,** 571–591.

Fewings, M., S. J. Lentz, and J. Fredericks, 2008: Observations of cross-shelf flow driven by cross-shelf winds on the inner continental shelf. *J. Phys. Oceanogr.,* **38,** 2358–2378.

Foken, T., 2006: 50 years of the Monin–Obukhov similarity theory. *Bound.-Layer Meteor.,* **119,** 431–447, doi:10.1007/s10546-006-9048-6.

Garrat, J. R., 1992: *The Atmospheric Boundary Layer.* Cambridge University Press, 316 pp.

Kantha, L. H., and C. A. Clayson, 1994: An improved mixed layer model for geophysical applications. *J. Geophys. Res.,* **99** (C12), 25 235–25 266.

Kundu, P. K., and I. M. Cohen, 2004: *Fluid Mechanics.* 3rd ed. Elsevier Academic Press, 759 pp.

Lentz, S. J., 1995: Sensitivity of the inner-shelf circulation to the form of the eddy viscosity profile. *J. Phys. Oceanogr.,* **25,** 19–28.

——, 2008: Seasonal variations in the circulation over the Middle Atlantic Bight continental shelf. *J. Phys. Oceanogr.,* **38,** 1486–1500.

—— and M. R. Fewings, 2012: The wind- and wave-driven inner-shelf circulation. *Annu. Rev. Mar. Sci.,* **4,** 317–343, doi:10.1146/annurev-marine-120709-142745.

——, ——, P. Howd, J. Fredericks, and K. Hathaway, 2008: Observations and a model of undertow over the inner continental shelf. *J. Phys. Oceanogr.,* **38,** 2341–2357.

Li, Z., and R. H. Weisberg, 1999a: West Florida shelf response to upwelling favorable wind forcing: Kinematics. *J. Geophys. Res.,* **104** (C6), 13 507–13 527.

—— and ——, 1999b: West Florida continental shelf response to upwelling favorable wind forcing. 2. Dynamics. *J. Geophys. Res.,* **104** (C10), 23 427–23 442.

Madsen, O. S., 1977: A realistic model of the wind-induced Ekman boundary layer. *J. Phys. Oceanogr.,* **27,** 248–255.

Mellor, G. L., and T. Yamada, 1982: Development of a turbulence closure model for geophysical fluid problems. *Rev. Geophys.,* **20,** 851–875.

Monin, A. S., and A. M. Obukhov, 1954: Basic laws of turbulent mixing in the ground layer of the atmosphere. *Tr. Geofiz. Inst., Akad. Nauk SSSR,* **151,** 163–187.

Pawlowicz, R., B. Beardsley, and S. Lentz, 2002: Classical tidal harmonic analysis including error estimates in MATLAB using T_TIDE. *Comput. Geosci.,* **28,** 929–937.

Shchepetkin, A. F., and J. C. McWilliams, 2005: The regional oceanic modeling system (ROMS): A split-explicit, free-surface, topography-following-coordinate oceanic model. *Ocean Modell.,* **9,** 347–404, doi:10.1016/j.ocemod.2004.08.002.

Simpson, J. H., J. Brown, J. Matthews, and G. Allen, 1990: Tidal straining, density currents, and stirring in the control of estuarine stratification. *Estuaries,* **13,** 125–132.

Stacey, M. T., and D. K. Ralston, 2005: The scaling and structure of the estuarine bottom boundary layer. *J. Phys. Oceanogr.,* **35,** 55–71.

——, J. R. Burau, and S. G. Monismith, 2001: Creation of residual flows in a partially stratified estuary. *J. Geophys. Res.,* **106** (C8), 17 013–17 037.

Stokes, G. G., 1847: On the theory of oscillatory waves. *Trans. Cambridge Philos. Soc.,* **8,** 441–455.

Tilburg, C. E., 2003: Across-shelf transport on a continental shelf: Do across-shelf winds matter? *J. Phys. Oceanogr.,* **33,** 2675–2688.

Zhang, W. G., G. G. Gawarkiewicz, D. J. McGillicuddy, and J. L. Wilkin, 2011: Climatological mean circulation at the New England shelf break. *J. Phys. Oceanogr.,* **41,** 1874–1893.